



3D Printing of Silk Protein Structures by Aqueous Solvent-Directed Molecular Assembly

Xuan Mu, Yu Wang, Chengchen Guo, Yamin Li, Shengjie Ling, Wenwen Huang, Peggy Cebe, Huan-Hsuan Hsu, Fabio De Ferrari, Xiaocheng Jiang, Qiaobing Xu, Alessandra Balduini, Fiorenzo G. Omenetto, and David L. Kaplan*

Hierarchical molecular assembly is a fundamental strategy for manufacturing protein structures in nature. However, to translate this natural strategy into advanced digital manufacturing like three-dimensional (3D) printing remains a technical challenge. This work presents a 3D printing technique with silk fibroin to address this challenge, by rationally designing an aqueous salt bath capable of directing the hierarchical assembly of the protein molecules. This technique, conducted under aqueous and ambient conditions, results in 3D proteinaceous architectures characterized by intrinsic biocompatibility/biodegradability and robust mechanical features. The versatility of this method is shown in a diversity of 3D shapes and a range of functional components integrated into the 3D prints. The manufacturing capability is exemplified by the single-step construction of perfusable microfluidic chips which eliminates the use of supporting or sacrificial materials. The 3D shaping capability of the protein material can benefit a multitude of biomedical devices, from drug delivery to surgical implants to tissue scaffolds. This work also provides insights into the recapitulation of solvent-directed hierarchical molecular assembly for artificial manufacturing.

silks,^[2,3] collagen tendons,^[4] cytoskeleton, and amyloid fibrils.^[5] This “bottom-up” strategy leads to ordered and hierarchical organization of molecules that further endows proteinaceous structures with the combination of inherent biological and exceptional material properties that are often difficult to obtain by artificial techniques using synthetic polymers.^[6] Furthermore, the natural processing strategy tactically excludes energy-intensive and harsh processing conditions that are used in industrial manufacturing and in the microfabrication of polymers, including high temperature/pressure, laser (two-photon and femtosecond), ultraviolet light, and organic solvents. In addition, artificial strategies to assemble molecules over hierarchical length scales usually focus on shape and size but not mechanical performance.^[7] Thus, artificial proteinaceous structures via directed molecular assembly are desired for nanotechnology,^[8,9] sustainable manu-

1. Introduction

A fundamental and ubiquitous manufacturing strategy in biology is the directed hierarchical molecular assembly in aqueous environments, which underlies the formation of various proteinaceous structures,^[1] such as spider and silkworm

facturing,^[10,11] and a wide range of biological and medical applications.^[12,13]

The biophysical mechanisms involved in the assembly/folding of protein molecules to form hierarchical structures are well known for the dependence on not only the primary amino

Dr. X. Mu, Dr. Y. Wang, Dr. C. Guo, Dr. Y. Li, Prof. S. Ling, Dr. W. Huang, Dr. H.-H. Hsu, F. De Ferrari, Prof. X. Jiang, Prof. Q. Xu, Prof. A. Balduini, Prof. F. G. Omenetto, Prof. D. L. Kaplan
Department of Biomedical Engineering
Tufts University
Medford, MA 02155, USA

E-mail: david.kaplan@tufts.edu

Dr. Y. Wang, F. De Ferrari, Prof. F. G. Omenetto
Silk lab, Tufts University
Medford, MA 02155, USA

Prof. S. Ling
School of Physical Science and Technology
ShanghaiTech University
Shanghai 201210, China

Prof. P. Cebe, Prof. F. G. Omenetto
Department of Physics and Astronomy
Tufts University
Medford, MA 02155, USA

Prof. A. Balduini
Department of Molecular Medicine
University of Pavia
Pavia 27100, Italy

Prof. F. G. Omenetto
Department of Electrical Engineering
Tufts University
Medford, MA 02155, USA

 The ORCID identification number(s) for the author(s) of this article can be found under <https://doi.org/10.1002/mabi.201900191>.

DOI: 10.1002/mabi.201900191

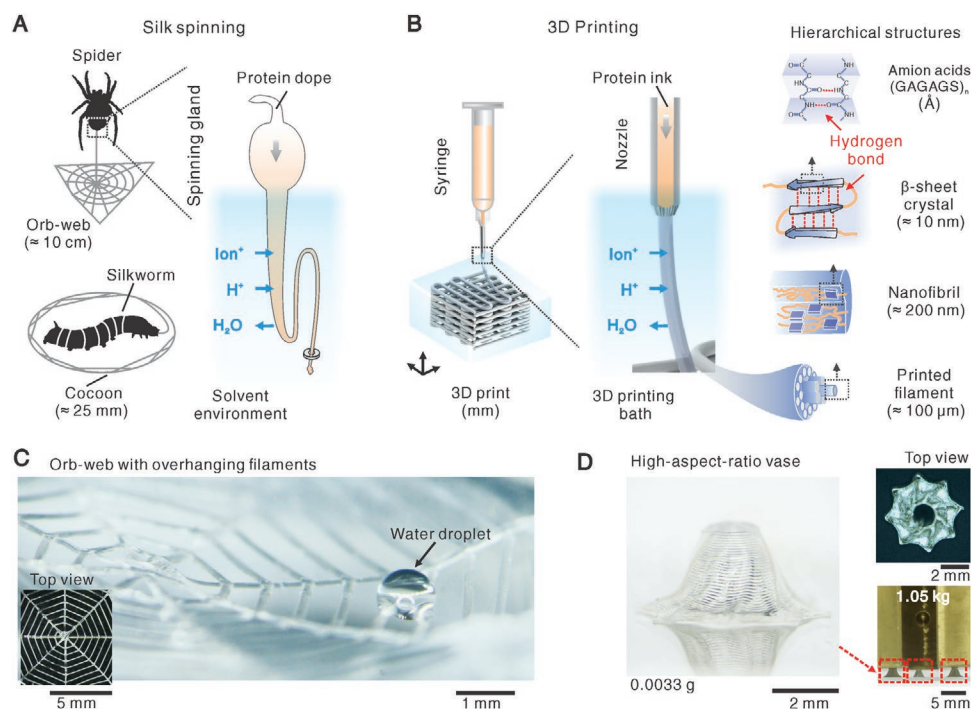


Figure 1. Bio-inspired 3D printing for a structural protein, regenerated silk fibroin. A) Schematic of solvent conditions along the spinning gland that direct the assembly of silk proteins for spinning silks into 3D macroscale orb-web and cocoons. B) Schematic of bioinspired 3D printing that uses a rationally devised aqueous salt bath to direct molecular assembly for constructing 3D ordered and hierarchical structures. G, glycine; A, alanine; S, serine. C) A printed two-layer overhanging orb-web composed of one arithmetic spiral and four radial straight lines in width of $\approx 100 \mu\text{m}$. A water droplet sits across two filaments. D) A printed vase ($\approx 0.0033 \text{ g}$) with high-aspect-ratio wall (≈ 26) and inward inclination ($\approx 63^\circ$). Three vases in total of $\approx 0.01 \text{ g}$ can support a six-order heavier load (1050 g) without breaking or delamination, suggesting the desired mechanical stability.

acid sequence,^[14] but also the aqueous solvent environment that is tightly and dynamically regulated by cells. For example, the assembly of silk proteins into macroscale orb-webs and cocoons is dictated by the gradient of several solvent conditions along the spinning gland, including shear stress,^[15] salt ions (like potassium and sodium),^[16–18] acidification,^[19,20] and dehydration (Figure 1A).^[21] The solvent conditions are crucial in the formation of proteinaceous structures in aspects of molecular conformational change and phase-transition; in particular, the salt ions can capture water molecules from the hydrated surface of silk fibroin, resulting in the transition of molecular conformation from random coil to β -sheet.^[22–25] The goal here was to recapitulate the aqueous solvent conditions for advanced digital manufacturing like three-dimensional (3D) printing, thus providing advantages in comparison to traditional manufacturing for automated fabrication of complex geometries and precise spatial-deposition of different materials.^[26]

However, it is not as straightforward as it may appear to translate the complicated *in vivo* solvent conditions into the artificial manufacturing of proteinaceous structures, aside from printing soft gels. In particular, most structures of silk proteins are manufactured in methanol bath/vapor.^[27–29] The methanol bath is compositionally different from the *in vivo* aqueous environment, leading to inferior control of molecular organization. Consequently, silk protein structures formed by 3D printing^[27] and molding/casting^[22] in methanol are rather brittle, in contrast to the natural, aqueous-derived counterparts. For the past decade, a handful of aqueous solutions, such as

ammonium sulfate^[30] and sodium acetate,^[31] have emerged for spinning 1D, mechanically strong silk fibers. These works provide useful insights into the wet-spinning of fibers,^[30–33] but are not extended to 3D printing.

From a broader perspective, many other mature 3D printing and artificial manufacturing approaches for various polymers may not be appropriate for manufacturing proteinaceous structures. For example, high temperature-induced phase-transition,^[34] covalent (chemical or photochemical) and ionic crosslinking,^[35,36] and reinforcing and supporting materials^[37,38] seem to deviate far from the aqueous solvent-based natural strategy and are generally insufficient to direct protein assembly, thus resulting in proteinaceous structures with either the mechanical performance severely inferior to that of natural counterparts, limited shaping capability, or both.^[39,40] For example, the thermoplastic processing of squid Suck Ring Teeth protein generated single fibers instead of 3D layered structures.^[34] The unsatisfied manufacturing capability restricts the potential of structural protein materials in comparison with the mature manufacturing of synthetic polymers. This challenging issue may be addressed by formulation of aqueous solvent conditions that are central to the molecular assembly and via emulating nature as reported here.

Herein, we develop a 3D printing technique of silk fibroin by the rational devising an aqueous solvent with inorganic salts. The relatively simple and acellular aqueous environment recapitulates crucial solvent conditions of silk spinning by both spiders and silkworms and thus is able to direct the hierarchical assembly of silk fibroin into 3D macroscale architectures with

intrinsic biocompatibility, mechanical strength and desired shape complexity (Figure 1B). As a proof of principle, the 3D shaping capability for the silk fibroin was demonstrated by a two-layer orb-web with overhanging structures and a vase with high-aspect-ratio wall and mechanical stability (Figure 1 C,D; Figure S1a, Supporting Information). Although focusing on one specific protein, silk fibroin, this work sets an example of using aqueous solvent environment to direct hierarchical molecular assembly for 3D printing and shows versatility by a range of printed shapes and multiple functional materials that can be integrated into the prints.

2. Results and Discussions

2.1. Silk Fibroin Ink

The silk fibroin was regenerated from the cocoon of mulberry silkworm *Bombyx mori*,^[41] embracing general characteristics of all silk proteins, such as repetitive short domains rich in glycine and/or alanine (like GAGAGS).^[42] The solution of silk fibroin, as printing ink, was a viscous yellowish clear liquid with $\approx 6\%$ β -sheet content, ≈ 30 wt% concentration, $\text{pH} \approx 7$, and ≈ 90 kDa molecular weight (Figure S1b,c, Supporting Information), analogous to native silk protein dope except for the lower molecular weight (≈ 90 kDa versus ≈ 300 kDa).^[41] The decreased molecular weight results from the cleavage of the polypeptide bonds at random sites during the regeneration of the silk fibroin, which includes degumming with boiling alkaline solution and dissolution with strong hydrogen-bond-destroying reagents. The processing time and the reagents used in degumming and dissolution have been harnessed to roughly control the molecular weight.^[43,44] Of note, the inherent genetic polymorphism of silk fibroin^[45] and the random cleavage determine the polydispersity of molecular weight. The hydrodynamic diameter of the diluted ink was around 23 nm, suggesting a single molecular dispersion (Figure S1c, Supporting Information).^[46] Rheological characterization of the ink showed typical shear-thinning behavior (Figure 2A; Figure S2, Supporting Information). We further used the Herschel–Bulkley (HB) model to fit viscous-shear rate profiles at the region of high shear rate ($>0.1 \text{ s}^{-1}$), as well as finite element analysis (FEA) to simulate the rheological behavior of the ink in the nozzle during 3D printing. At a printing pressure of 210 kPa, the viscosity decreased by nearly a hundred-fold (from 547.22 to 6.18 Pa·s) and the simulated shear rate reached $\approx 65 \text{ s}^{-1}$, above in vivo critical values ($\approx 1\text{--}10 \text{ s}^{-1}$),^[47] indicating the elongation of protein molecules during 3D printing, mimicking native silk spinning.^[15]

2.2. De Novo Aqueous Salt Bath

As the crux of this work, we rationally developed an aqueous bath with a de novo composition of inorganic salts (0.5 M dipotassium phosphate and 4 M sodium chloride) to recapitulate solvent conditions of silk spinning by two evolutionarily distant species—spiders and silkworms. The chemical composition

as well as the working mechanism to solidify ink of this bath are essentially different from others for wet spinning and 3D printing for proteins and polymers (Table S1, Supporting Information). First, the bath is an aqueous solution composed of the most abundant salt ions in the spinning glands, such as potassium and sodium,^[16,25] which contrasts to baths of methanol and ammonium sulfate. We assume that the metal ions participate in the spinning of silks, perhaps by imposing specific effects on proteins through interacting with water molecules on the protein surfaces ref. [18] other than forming ionic bonds. Second, the bath is of a slightly acidic pH (≈ 6) and high osmolarity ($>8 \text{ M}$, as one sodium chloride molecule disassociates into two ions) to remove water from extruded ink, which recapitulates solvent conditions of acidification^[19,20] and dehydration^[21] for silk spinning. Notably, in comparison with the osmolarity of 0.9 wt % normal saline (0.308 M), the high osmolarity is not isotonic and seems non-physiological, but the elevation of the osmolarity is indeed a general principle found in animals for concentrating urine, that is, dehydration.^[48] Because the exact concentration of ions at the site of silk fiber formation remains unknown,^[49] it is difficult to evaluate the difference in osmolarity between the bath and the natural spinning gland. Third, the bath results in the crosslinking and phase separation of the silk fibroin. The crosslinking dynamics are optimized for 3D printing, tightly related to the phase-transition of the ink from liquid to gel, by characterizing the change of storage modulus (G') (Figure 2B). Two extremes of high (10 M) and low (zero) concentrations of potassium ions led to a dramatic increase (≈ 1000 -fold) of G' that is prone to clog the nozzle and slight decrease (≈ 0.5 -fold) that cannot support shape retention, respectively. So, these formulations and the consequent assembly dynamics are unfavorable for 3D printing. While the optimized bath with 0.5 M potassium resulted in a relatively moderate increase of G' (≈ 14 -fold from 1.05 Pa to 14.4 Pa within ≈ 2 min). Of note, this balanced dynamics led to shape retention, continuous extrusion and adherence of multiple layers, thus enabling the 3D printing of the protein ink (Movies S1–S4, Supporting Information). The balanced assembly dynamics also distinguishes this work from other state-of-the-art fiber spinning.^[30–33]

2.3. Ordered and Hierarchical Structure

Ordered hierarchical organization of molecules is a characteristic of directed molecular assembly (Figure 1B). The 3D prints were first washed with DI water to remove the salts, as shown by energy dispersive spectroscopy (EDS) in Figure S1, Supporting Information. In the absence of ionic bonds, the removal of the salt ions will not influence the structural integrity of the prints, in sharp contrast to the alginate prints that will collapse after chelating ions. Fourier transform infrared spectroscopy (FTIR) spectra demonstrated that the aqueous salt bath transforms the silk fibroin from random coil/helix to β -sheet after printing with an approximate eight-fold increase from $\approx 6\%$ to $\approx 48\%$ (Figure 2C). Silk fibroin molecules assembled through the stacking of the repetitive domain (GAGAGS) with the formation of hydrogen bonds, notable as physical crosslinks without chemical or photochemical crosslinking

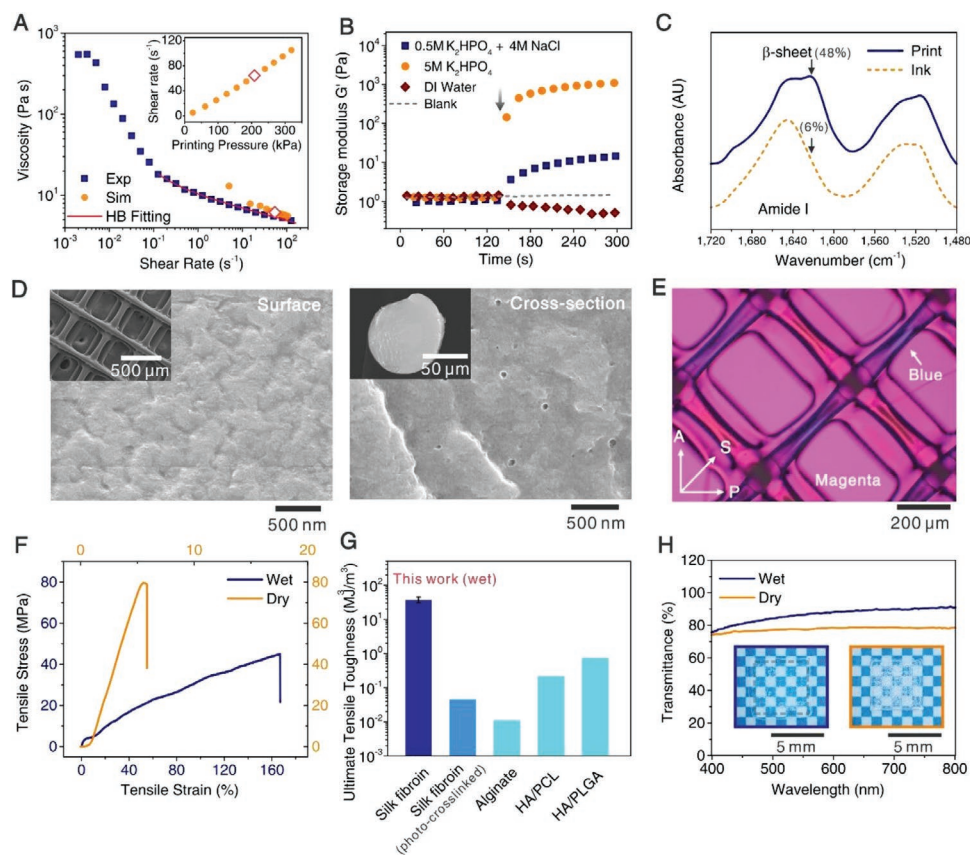


Figure 2. Structural characterizations of printing ink and 3D prints. A) Viscosity-shear rate profile of the protein ink, Herschel–Bulkley (HB) model and finite element analysis (FEA) simulation. Red hollow diamonds indicate printing pressure of 210 kPa. Inset, simulated shear rate versus printing pressure. B) Oscillatory time sweep of the protein ink to show the dynamics of molecular assembly. An arrow indicates the addition of solutions with different potassium concentrations. C) Fourier transform infrared spectroscopy (FTIR) of the protein ink and the print. The numbers in brackets indicate semi-quantitative content of β -sheet. D) Scanning electron microscope (SEM) images of 3D printed structure and the cross-section fractured in liquid nitrogen. E) Blue filament against magenta background indicates the longitudinal molecular alignment. A, P, and S indicate analyzer, polarizer, and the slow axis of the first order red plate, respectively. F) Typical uniaxial tensile stress–strain curves of single fibers from a seven-layer 3D print (more details in Figure S4d, Supporting Information). G) The ultimate tensile toughness of this work is compared with that of photo-crosslinked silk fibroin, ionic-crosslinked polysaccharide (alginate), synthetic composite biopolymers (hydroxyapatite-polycaprolactone, HA/PCL and hydroxyapatite/poly(lactide-co-glycolic acid), HA/PLGA). All samples are tested in wet. Error bar represents standard deviation with three repeats. H) Transmittance curves and images of 3D prints. A 3D printed membrane with ≈ 0.1 mm thickness is used for transmittance measurement. Grey dash line indicates the boundary.

requirements. Scanning electron microscopy (SEM) images of the cross-sections of a filament, fractured by tensile force, showed that the assembled molecules aggregated into nanofibrils (≈ 200 nm in diameter) (Figure S4c,d, Supporting Information); the individual nanofibrils seem to be pulled out. And SEM images of another filament, fractured in liquid nitrogen, showed nanofibrils densely packed into solids with an almost homogeneous morphology at the nanoscale (Figure 2D). Sparse nanoholes in the cross-sections were probably caused by residual water. The homogeneous molecular conformation was also confirmed by Raman spectral mapping across the full width of a filament, which showed the almost unvaried distribution of β -sheet and perhaps exclude a core-shell structure (Figure S3c,d, Supporting Information). Moreover, birefringence images demonstrated longitudinal alignment of the protein molecular chains including both amorphous and crystalline regions (Figure 2E, Figure S3a–e, Supporting Information).

2.4. Mechanic and Optic Performance

A 3D printed four-layer lattice (in wet) is of compliance, extensibility, and durable junctions between layers that remain intact under repeatedly stretching and folding (Figure S4c and Movie S4, Supporting Information). The structure of the print remains stable for at least several months owing to the secondary structure of crystalline β -sheet. To characterize the mechanical performance in uniaxial tensile tests, single filaments of ≈ 30 mm in length were directly cut from a seven-layer 3D print without post-stretching (Figure 2F; Figure S4a,d, Supporting Information). The prints demonstrated different mechanical behaviors in dry and wet conditions, both of which are useful and optional for different applications. Besides air drying, a range of commercial techniques including lyophilization (Lyo) and critical point drying (CPD) can be used to dry the prints after removing the salts. Of note, Lyo and CPD preserve the morphology while air drying causes an almost isotropic shrink of the structure by

≈15% (Figure S1f, Supporting Information). Generally, water molecules make proteinaceous prints less stiff but more extensible. Ultimate tensile strength (39 ± 8 MPa, wet) of the print outperformed that of both photo-crosslinked (0.075 ± 0.0075 MPa, wet)^[35] and organic solvent-processed silk fibroin ($0.08\text{--}0.7$ MPa, wet)^[50] by 2–3 orders of magnitude (there is no tensile test results of 3D printed silk fibroin in methanol^[27] for comparison); moreover, ultimate tensile toughness (37 ± 7 MJ m⁻³, wet) was higher than that of all other 3D printed polymers ranging from 0.2 to 27.6 MJ m⁻³ (Figure 2G; Figure S4f and Table S2, Supporting Information). The toughness of the filament as part of 3D prints was superior to or comparable with natural and artificial fibers (native silkworm silk, ≈70 MJ m⁻³; flax,^[51] 7–14 MJ m⁻³; supramolecular fiber,^[11] 22.8 ± 10.3 MJ m⁻³; and recombinant silk fiber,^[31] 45 ± 7 MJ m⁻³). The high toughness rendered 3D prints capable of absorbing significant energy prior to fracture, which is desired for prey trapping and some applications. Of note, the tensile strength and toughness are the intrinsic material properties, while the mechanical properties of the print depend on the material as well as the organization of the printed filament. Also, the improved mechanical performance results from the ordered hierarchical structures, and highlights the distinctive capability of solvent-directed molecular assembly in comparison with, for example, methanol bath and chemical and photochemical crosslinking. In addition, the absence of intensive energy input (like temperature-induced phase transition) during 3D printing makes the resulting mechanical performance particularly compelling.

The dense morphology allows 3D prints visually transparent, such as the vase (Figure 1D; Figure S5, Supporting Information) and lattice and membrane (Figure 2h), promising for levitating bio-photonics applications to 3D.^[52] For measuring transmittance, we used 3D printed ≈0.1 mm-thick membranes

composed of parallel and contiguous filaments (Figure 2H). The transmittance in both dry and wet states was above 80% from 400 to 800 nm, comparable to previous results of proteinaceous structures fabricated by 2D manufacturing like spinning coating or film casting.^[52]

2.5. Biocompatible and Multi-Material Printing

The whole process of 3D printing is at ambient and aqueous conditions, which is highly desired to preserve the biodegradability and cytocompatibility as well as the integrated biofunctions of 3D proteinaceous prints, because harsh processing conditions and toxic organic solvent probably deteriorate these properties. The biodegradability was investigated in the proteolytic degradation of the prints (Figure 3A). Proteolytic degradation is the enzyme-controlled breakdown of silk fibroin into short polypeptides and amino acids, which is advantageous to potentially feed cells with amino acids and to avoid rapid local acidification, in contrast to the chemical hydrolysis of synthetic polyesters such as poly(lactic-co-glycolic acid) (PLGA). Two post-processing techniques, including CPD and Lyo, result in different degradation profiles, due to the different levels of protein crystallinity, thus offering an option to tune the degradation dynamics. The cytocompatibility was shown by the confluent layer of human umbilic vein endothelial cells; endothelialization (Figure S6, Supporting Information). Of note, the designated biomedical applications of the silk prints with filament diameters of ≈100 microns are different from scaffolds with filament diameters below tens of microns. The printing ink allows a wide range of additives, including quantum dots, small fluorescent molecules, and especially bioactive horseradish peroxidase (HRP), to render 3D prints additional functions (Figure 3B,C;

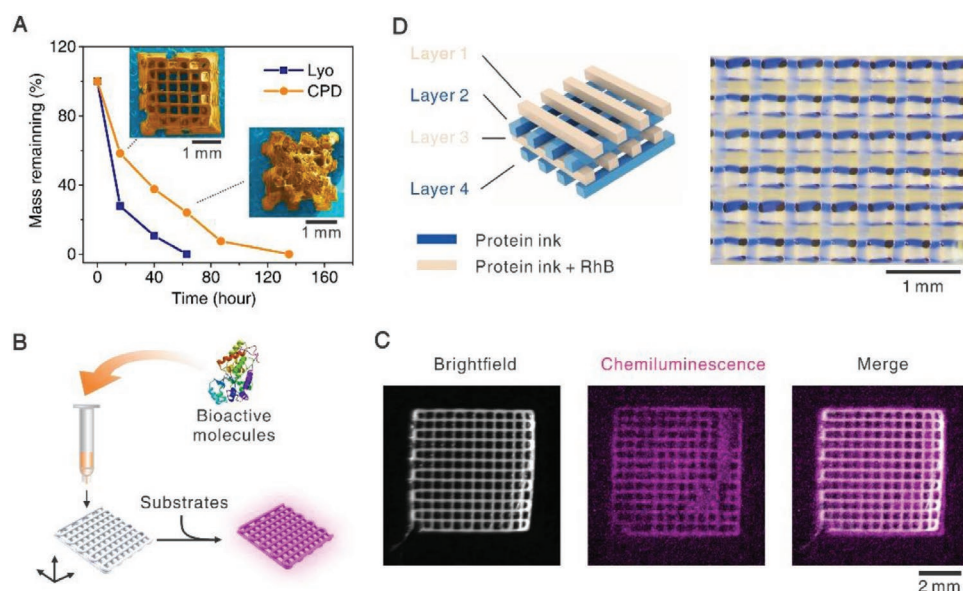


Figure 3. Enzymatic/proteolytic degradation, integration of biofunctions, and multi-material printing. A) Profiles and images of in vitro enzymatic degradation of 39-layer rectangle lattices processed by lyophilization or critical point drying (CPD). B) Schematic of integrating multiple functional additives (like horseradish peroxidase, HRP) into 3D prints. C) A 3D print emits chemiluminescence with substrates (Luminol and H₂O₂) to show the preserved activity of HRP. D) Schematic and fluorescent image (under UV light) of a 3D printed four-layer lattice with spatially programmed rhodamine B (RhB). The blue is due to the reflection of near-UV light.

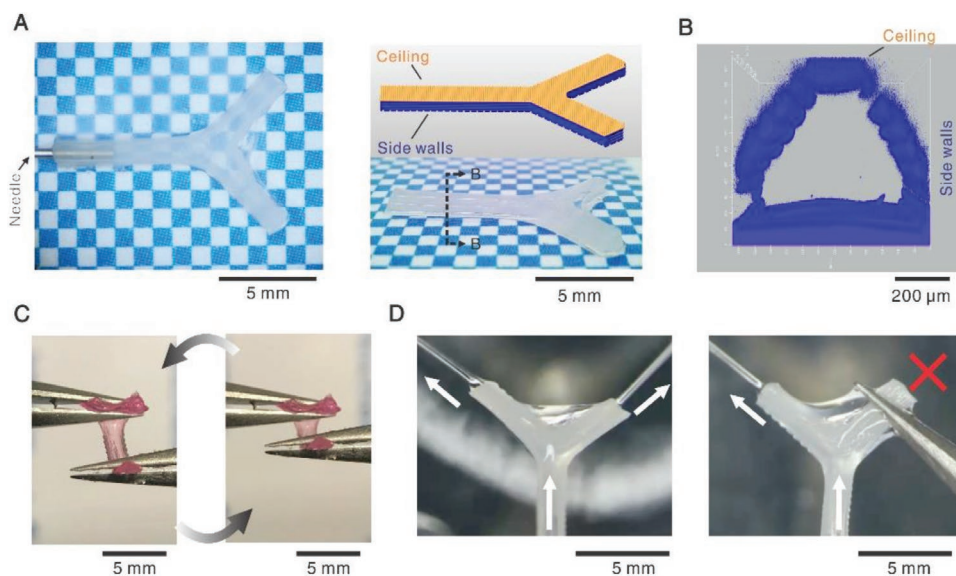


Figure 4. Single-step 3D printing of bifurcated microfluidic channels. A) Images and design of 3D printed microfluidic channel. A 25 Gauge needle, slightly larger than the inner diameter of the channel, can be conveniently inserted for tubing. B) Confocal image of the cross-section of the main channel. C) Microfluidic channel (in red dye) under repeatedly bending over a large curvature, indicating structural integrity. D) Microfluidic channel enables high flow rate ($\approx 0.5 \text{ mL s}^{-1}$) and can be controlled by pinching with tweezers. White arrows and red cross indicate water jets and closure, respectively.

Figure S7, Supporting Information). Due to the phase separation of the crosslinked silk fibroin, as well as hydrophobic/electronic interactions, doped materials are largely maintained in the silk structure with minimized leaking into the bath (Figure S7e, Supporting Information). The enzymatic activity of horseradish peroxidase integrated into a two-layer 3D print allows emitting in the presence of enzyme substrates. Of note, it is advantageous of this work to eliminate the use of methanol bath^[27] because methanol reduces the activity of horseradish peroxidase in silk films nearly fourfold.^[53] The doped silk prints may be dried for convenient transport and long-term stability of water-sensitive additives; the drying technique can thus be chosen on the basis of the sensitivity of the additives. Lyophilization has been widely used for being almost harmless to the activity of a plethora of pharmaceutical/ biopharmaceutical products. In addition, silk fibroin materials in the dry state preserve the activity of some doped functional additives,^[53] an extra benefit for the 3D silk prints. Considering an array of well-established composite silk fibroin materials, we envision the doping of these additives will not influence the structural stability and integrity, as well as more additives such as graphene^[54] and antibiotics^[55] can be integrated into the proteinaceous 3D prints. Furthermore, the capability of programming multi-materials with special precision into functionally heterogeneous architectures is common in nature and nontrivial in many artificial applications, which was exemplified by printing an alternate pattern of fluorescence into 3D proteinaceous structures (Figure 3D).

2.6. Microfluidic Channels

We further demonstrated the manufacturing capability by constructing a bifurcate and perfusable microfluidic channel in a

single-step manner (Figure 4; Movie S5, Supporting Information). A structure like the microfluidic channel places stringent demands on the printing capability; the printed structures are overhanging at the ceiling and high aspect-ratio at the sidewall. Besides, the two types of structures require rapid assembly dynamics to prevent subsidence and relatively slow assembling dynamics to form seamless and water-proof adherence between sequentially extruded filaments, respectively. Along with the optimized assembly dynamics, we addressed these demanding requirements by using compartmentalized priming parameters. For bottom layers and side walls, the printing speed and pressure was 1 mm s^{-1} and $\approx 210 \text{ kPa}$, respectively; while for building the ceiling layer, the printing speed and pressure was elevated to 1.5 mm s^{-1} and $\approx 250 \text{ kPa}$, respectively. Of note, this work eliminated the use of sacrificial and supporting materials to significantly streamline the manufacturing of complex and hollow shapes.^[56,57] The printed ten-layer microfluidic channels demonstrated high resolution ($\approx 350 \text{ }\mu\text{m}$ diameter and $\approx 100 \text{ }\mu\text{m}$ wall thickness), elasticity, mechanical stability, and desired perfusability. The channel thus can be reversibly bent over a large curvature (Figure 4D) and controlled with a pinch-based valve (Figure 4E). The backpressure of the microfluidic channel was up to 300 kPa , which covers the range of most applications of microfluidics as well as physiological blood pressures, promising for constructing artificial vascular grafts. Indeed, the silk is particularly suitable for constructing small-diameter vascular grafts ($<6 \text{ mm}$), because unlike synthetic polymers such as poly-tetrafluoroethylene and poly(ethylene terephthalate) does not facilitate thrombus formation and intimal hyperplasia.^[58] Furthermore, 3D printing offers significant manufacturing flexibility in comparison with other techniques, including soft lithography, spinning, and coatings, for microfluidic chips and proteinaceous vascular grafts.

3. Conclusions

This work aims at the recapitulation of the fundamental natural manufacturing strategy beyond the mere reconstruction of 3D proteinaceous structures. The general solvent conditions for silk spinning by two species with distant origins and independent evolutions, spiders and silkworms, inspired us to devise the de novo aqueous salt bath. The particular composition of salt ions was valuable to direct silk fibroin assembly for 3D printing. In addition, the ambient and aqueous processing and the renewable protein materials utilized, in comparison with high temperature/pressure and petroleum-derived materials, are expected to consume minimum energy and generate negligible waste, thus taking a preliminary yet promising step to sustainable manufacturing of polymers. This work combines the intrinsic merits of protein materials and the shape versatility of 3D printing, opening up new opportunities for constructing various proteinaceous structures, and presenting a promising alternative to widely used manufacturing techniques with synthetic polymers.

4. Experimental Section

The protein ink was prepared using concentrated solution of regenerated silk fibroin, according to previous methods^[41] with modifications. The protein ink was characterized by dynamic light scattering (DLS, ZetaPALS, Brookhaven), Fourier transform infrared spectroscopy (FTIR) in ATR mode (FTIR-6200, Jasco Instruments, Easton, MD), rheometry (ARES-LS2, TA Instruments, New Castle, DE) and pH meter. 3D printing was performed with an Inkredible printer (Cellink, Sweden) using compressed air to extrude the protein ink, loaded in a 3 mL syringe, through a 33-gauge chamfered dispensing nozzle onto the bottom surface (a glass slide) of a reservoir that is filled with the aqueous salt bath (4 M sodium chloride and 0.5 M dipotassium phosphate). The printing path was controlled by manually written G-code commands. The printing speed (moving speed of printing head) and pressure is 1 mm s⁻¹ and 210 kPa, respectively, unless stated otherwise. The assembly dynamics is investigated by oscillatory time sweep at 1 Hz and 1% strain (within the linear viscoelastic region) for 5 min. The printed structure were rinsed with DI water and dried by either air, lyophilization or critical point drying, and characterized by FTIR, Raman microspectroscopy (Horiba Multiline Raman Spectrometer, Horiba scientific, Japan), scanning electron microscopy (Ultra 55 field-emission SEM, Carl Zeiss AG, Germany) with EDS detector, polarized optical microscopy (Eclipse E200POL, Nikon, Japan), uniaxial tensile test (Instron 3366, Instron, USA), and light transmission measurement (vis/near-infrared fiber-optic spectrometer, USB-2000, Ocean Optics, USA). In vitro enzymatic degradation of the 3D prints was evaluated at 37 °C in 5 U Pronase E solution, an unusual nonspecific protease (P8811, Sigma-Aldrich), according to previous work.^[22] Primary Human umbilical vein endothelial cells (HUVECs, C2519A, Lonza) were cultured on 3D prints for endothelialization and were imaged (Leica SP8 confocal microscope, Leica microsystems, Germany).

Supporting Information

Supporting Information is available from the Wiley Online Library or from the author.

Acknowledgements

The authors thank the NIH (P41EB002520, R01AR068048, U01EB014976, R01NS092847, R01DE016525, R01EB016041-02), the NSF

(IOS-1557672), the AFOSR (FA9550-17-1-0333), the ONR (N00014-16-1-243), and the Paul G. Allen Foundation (2171) for support of this work; the authors acknowledge the Harvard University Center for Nanoscale Systems (CNS) for providing SEM and other measurements. The CNS is a member of the National Nanotechnology Coordinated Infrastructure Network (NNCI), which is supported by the NSF (1541959).

Conflict of Interest

The authors declare no conflict of interest.

Keywords

3D printing, microfluidics, salt ions, self-assembly, silk fibroin

Received: May 29, 2019

Revised: July 15, 2019

Published online: August 21, 2019

- [1] S. Zhang, *Nat. Biotechnol.* **2003**, *21*, 1171.
- [2] F. G. Omenetto, D. L. Kaplan, *Science* **2010**, *329*, 528.
- [3] M. J. Buehler, Y. C. Yung, *Nat. Mater.* **2009**, *8*, 175.
- [4] K. E. Kadler, A. Hill, E. G. Canty-Laird, *Curr. Opin. Cell Biol.* **2008**, *20*, 495.
- [5] T. P. Knowles, R. Mezzenga, *Adv. Mater.* **2016**, *28*, 6546.
- [6] J. M. Gosline, *Mechanical Design of Structural Materials in Animals*, Princeton University Press, Princeton, NJ **2018**.
- [7] H. Qiu, Z. M. Hudson, M. A. Winnik, I. Manners, *Science* **2015**, *347*, 1329.
- [8] R. V. Ulijn, R. Jerala, *Chem. Soc. Rev.* **2018**, *47*, 3391.
- [9] B. A. Grzybowski, W. T. Huck, *Nat. Nanotechnol.* **2016**, *11*, 585.
- [10] M. Garetti, M. Taisch, *Production Planning Control* **2012**, *23*, 83.
- [11] Y. Wu, D. U. Shah, C. Liu, Z. Yu, J. Liu, X. Ren, M. J. Rowland, C. Abell, M. H. Ramage, O. A. Scherman, *Proc. Natl. Acad. Sci. U. S. A.* **2017**, *114*, 8163.
- [12] C. H. Lee, A. Singla, Y. Lee, *Int. J. Pharm.* **2001**, *221*, 1.
- [13] C. Holland, K. Numata, J. Rnjak-Kovacina, F. P. Seib, *Adv. Healthcare Mater.* **2019**, *8*, 1800465.
- [14] P.-S. Huang, S. E. Boyken, D. Baker, *Nature* **2016**, *537*, 320.
- [15] C. Holland, A. Terry, D. Porter, F. Vollrath, *Nat. Mater.* **2006**, *5*, 870.
- [16] F. Hagn, L. Eisoldt, J. G. Hardy, C. Vendrely, M. Coles, T. Scheibel, H. Kessler, *Nature* **2010**, *465*, 239.
- [17] E. Degtyar, M. J. Harrington, Y. Politi, P. Fratzl, *Angew. Chem., Int. Ed.* **2014**, *53*, 12026.
- [18] H. I. Okur, J. Hladílková, K. B. Rembert, Y. Cho, J. Heyda, J. Dzubiella, P. S. Cremer, P. Jungwirth, *J. Phys. Chem. B* **2017**, *121*, 1997.
- [19] L. Domigan, M. Andersson, K. Alberti, M. Chesler, Q. Xu, J. Johansson, A. Rising, D. Kaplan, *Insect Biochem. Mol. Biol.* **2015**, *65*, 100.
- [20] G. Askarieh, K. Nordling, A. Saenz, C. Casals, A. Rising, J. Johansson, S. D. Knight, *Nature* **2010**, *465*, 236.
- [21] H.-J. Jin, D. L. Kaplan, *Nature* **2003**, *424*, 1057.
- [22] U.-J. Kim, J. Park, H. J. Kim, M. Wada, D. L. Kaplan, *Biomaterials* **2005**, *26*, 2775.
- [23] Q.-X. Ruan, P. Zhou, *J. Mol. Struct.* **2008**, *883–884*, 85.
- [24] Q. X. Ruan, P. Zhou, B. W. Hu, D. Ji, *FEBS J.* **2008**, *275*, 219.
- [25] L. Zhou, X. Chen, Z. Shao, Y. Huang, D. P. Knight, *J. Phys. Chem. B* **2005**, *109*, 16937.



- [26] R. L. Truby, J. A. Lewis, *Nature* **2016**, *540*, 371.
- [27] S. Ghosh, S. T. Parker, X. Wang, D. L. Kaplan, J. A. Lewis, *Adv. Funct. Mater.* **2008**, *18*, 1883.
- [28] B. Marelli, N. Patel, T. Duggan, G. Perotto, E. Shirman, C. Li, D. L. Kaplan, F. G. Omenetto, *Proc. Natl. Acad. Sci. U. S. A.* **2017**, *114*, 451.
- [29] P. Tseng, B. Napier, S. Zhao, A. N. Mitropoulos, M. B. Applegate, B. Marelli, D. L. Kaplan, F. G. Omenetto, *Nat. Nanotechnol.* **2017**, *12*, 474.
- [30] G. Zhou, Z. Shao, D. P. Knight, J. Yan, X. Chen, *Adv. Mater.* **2009**, *21*, 366.
- [31] M. Andersson, Q. Jia, A. Abella, X.-Y. Lee, M. Landreh, P. Purhonen, H. Hebert, M. Tenje, C. V. Robinson, Q. Meng, G. R. Plaza, J. Johansson, A. Rising, *Nat. Chem. Biol.* **2017**, *13*, 262.
- [32] A. Koepfel, C. Holland, *ACS Biomater. Sci. Eng.* **2017**, *3*, 226.
- [33] Y. Liu, J. Ren, S. Ling, *Composites Commun.* **2019**, *13*, 85.
- [34] V. Latza, P. A. Guerette, D. Ding, S. Amini, A. Kumar, I. Schmidt, S. Keating, N. Oxman, J. C. Weaver, P. Fratzl, A. Miserez, A. Masic, *Nat. Commun.* **2015**, *6*, 8313.
- [35] S. H. Kim, Y. K. Yeon, J. M. Lee, J. R. Chao, Y. J. Lee, Y. B. Seo, M. T. Sultan, O. J. Lee, J. S. Lee, S.-i. Yoon, *Nat. Commun.* **2018**, *9*, 1620.
- [36] T. J. Hinton, Q. Jallerat, R. N. Palchesko, J. H. Park, M. S. Grodzicki, H.-J. Shue, M. H. Ramadan, A. R. Hudson, A. W. Feinberg, *Sci. Adv.* **2015**, *1*, e1500758.
- [37] H.-W. Kang, S. J. Lee, I. K. Ko, C. Kengla, J. J. Yoo, A. Atala, *Nat. Biotechnol.* **2016**, *34*, 312.
- [38] M. R. Sommer, M. Schaffner, D. Carnelli, A. R. Studart, *ACS Appl. Mater. Interfaces* **2016**, *8*, 34677.
- [39] M. K. Włodarczyk-Biegun, A. del Campo, *Biomaterials* **2017**, *134*, 180.
- [40] L. Moroni, J. A. Burdick, C. Highley, S. J. Lee, Y. Morimoto, S. Takeuchi, J. J. Yoo, *Nat. Rev. Mater.* **2018**, *3*, 21.
- [41] D. N. Rockwood, R. C. Preda, T. Yücel, X. Wang, M. L. Lovett, D. L. Kaplan, *Nat. Protoc.* **2011**, *6*, 1612.
- [42] M. Andersson, J. Johansson, A. Rising, *Int. J. Mol. Sci.* **2016**, *17*, 1290.
- [43] Q. Wang, Q. Chen, Y. Yang, Z. Shao, *Biomacromolecules* **2013**, *14*, 285.
- [44] L. S. Wray, X. Hu, J. Gallego, I. Georgakoudi, F. G. Omenetto, D. Schmidt, D. L. Kaplan, *J. Biomed. Mater. Res., Part B* **2011**, *99B*, 89.
- [45] P. Laity, S. Gilks, C. Holland, *Polymer* **2015**, *67*, 28.
- [46] K. S. Hossain, A. Ochi, E. Ooyama, J. Magoshi, N. Nemoto, *Biomacromolecules* **2003**, *4*, 350.
- [47] D. N. Breslauer, L. P. Lee, S. J. Muller, *Biomacromolecules* **2009**, *10*, 49.
- [48] T. Berl, *Trans. Am. Clin. Climatol. Assoc.* **2009**, *120*, 389.
- [49] A. Rising, J. Johansson, *Nat. Chem. Biol.* **2015**, *11*, 309.
- [50] Z. Zhu, S. Ling, J. Yeo, S. Zhao, L. Tozzi, M. J. Buehler, F. Omenetto, C. Li, D. L. Kaplan, *Adv. Funct. Mater.* **2018**, *28*, 1704757.
- [51] D. U. Shah, D. Porter, F. Vollrath, *Compos. Sci. Technol.* **2014**, *101*, 173.
- [52] F. G. Omenetto, D. L. Kaplan, *Nat. Photonics* **2008**, *2*, 641.
- [53] S. Lu, X. Wang, Q. Lu, X. Hu, N. Uppal, F. G. Omenetto, D. L. Kaplan, *Biomacromolecules* **2009**, *10*, 1032.
- [54] S. Ling, Q. Wang, D. Zhang, Y. Zhang, X. Mu, D. L. Kaplan, M. J. Buehler, *Adv. Funct. Mater.* **2018**, *28*, 1704757.
- [55] E. M. Pritchard, T. Valentin, B. Panilaitis, F. Omenetto, D. L. Kaplan, *Adv. Funct. Mater.* **2013**, *23*, 854.
- [56] K. Zhu, N. Chen, X. Liu, X. Mu, W. Zhang, C. Wang, Y. S. Zhang, *Macromol. Biosci.* **2018**, *18*, 1800127.
- [57] M. A. Heinrich, W. Liu, A. Jimenez, J. Yang, A. Akpek, X. Liu, Q. Pi, X. Mu, N. Hu, R. M. Schiffelers, *Small* **2019**, *15*, 1970126.
- [58] T. Asakura, T. Tanaka, R. Tanaka, *ACS Biomater. Sci. Eng.* **2019**, <https://doi.org/10.1021/acsbiomaterials.8b01482>.